Supporting Information for "The composition of the deep continental crust inferred from geochemical and geophysical data"

L. G. Sammon[1], W. F. McDonough[1,2], W. Mooney[3]

[1]Department of Geology, University of Maryland, College Park, MD 20742, USA

[2]Department of Earth Sciences and Research Center for Neutrino Science, Tohoku University, Sendai 980-8578, Japan

[3]Earthquake Science Center, United States Geological Survey, Menlo Park, CA 94025

Contents of this file

1. List of data inputs and models used to build our global deep crust model
2. Perple_X parameter settings and justification
3. Figures S1 to S18, global maps of major oxide composition at two depths

Additional Supporting Information (Files uploaded separately)

1. Collection of scripts and files for running CrustMaker
2. Global SiO_2 vs. depth model file

1. Deep Crustal Modeling

CrustMaker scripts/code - link here Geochemical Dataset - link here

USGS seismic dataset - please contact Walter Mooney at mooney@usgs.org. Global deep crust seismic data was compiled from a survey of 8000 literature based vertical seismic profiles (W. D. Mooney et al., 1998). Only profiles with both Vp and Vs were considered. The profiles were collected by various controlled and passive source methods, including refraction (reversed and unreversed), earthquake models, receiver functions, and ambient noise tomography. This data includes estimates of sediment thickness and elevation.

Global gravity anomalies from GRACE and GOCE - (Ries et al., 2016) Crustal thickness = (Pasyanos et al., 2014; Szwillus et al., 2019) Surface heat flow - (Lucazeau, 2019; Shen et al., 2020)

2. PerpleX Modeling Parameters

Parameter - *Value* - Justification

Thermodynamic data file - *Hpha02ver.dat: Holland and Powell thermodynamic database, augmented by Hacker and Abers (2004)* - Holland and Powell (2004) presents a self-consistent thermodynamic database. Hpha02ver is similar to hp02ver but is augmented by Hacker and Abers (2004) to be consistent with the α - β quartz transition. Another option, Hp11ver.dat, does not include shear moduli and thus cannot be used to calculate Vs. The Stx11ver.dat database uses the Stixrude and Lithgow-Bertelloni (2011) method for calculating elastic moduli, but only considers major mantle phases.

Solution models - *N/A* - No solution models were included. Including solution models increases the calculation time 13-fold. The difference between results when not including solution models vs. including Holland & Powell (HP) solution models averages to 0.1 km/s in Vp, <0.1 km/s in Vs, and <0.01 in Vp/Vs. Future tests including solution models can report on the accuracy of mineral endmember solutions, but this does not measurably change bulk rock and bulk crustal properties.

Amphibolite Volatiles - *1 wt.%* - The median amount of H_2O in amphibolite samples (N = 285) was found to be 1.2 $\pm$ 0.6 wt.%. 1 wt.% was chosen as a starting point calculation. Further calculations can be done with 0.5 wt.% and 1.5 wt.% water.

Pressure Range - *1,500 - 30,000 bars (0.15 - 3.0 GPa)* - This range translates to depths from about 5km to 100km, which encompasses the amphibolite and granulite stability fields and expected deep crustal depths up to Himalayan thickness.

Temperature Range - *300 - 1800 K (27 - 1,027°C)* - Temperatures below 770 K covers near-surface temperatures to the amphibolite stability field, in case amphibolites exist in the middle crust in disequilibrium. 800 - 1300 K encompasses the stability field for granulite. 300 - 800 covers all possibilities from near-surface temperatures to the granulite wet solidus. Granulites existing in this range would be at thermodynamic disequilibrium, but retrograde metamorphosis is unlikely. Granulite facies metamorphosis is marked by the dehydration of hydrous minerals. Rehydration is difficult, making rehydration unlikely to occur (Semprich & Simon, 2014). 1800 K sets the (very hot) maximum temperature

cap to again account for possible temperatures in Himalayan crust and also to allow room for experimentation with temperature.

Granulite Volatiles - *0 wt.%* - Granulite is characterized by the dehydration of hydrous minerals.

3. Major Oxide Maps

References

Artemieva, I. M. (2006). Global 1×1 thermal model TC1 for the continental lithosphere: implications for lithosphere secular evolution. *Tectonophysics*, *416*(1-4), 245–277.

Ashwal, L., Morgan, P., Kelley, S., & Percival, J. (1987). Heat production in an Archean crustal profile and implications for heat flow and mobilization of heat-producing elements. *Earth and Planetary Science Letters*, *85*(4), 439–450.

Caldwell, W. B., Klemperer, S. L., Rai, S. S., & Lawrence, J. F. (2009). Partial melt in the upper-middle crust of the northwest himalaya revealed by rayleigh wave dispersion. *Tectonophysics*, *477*(1-2), 58–65.

Cammarano, F., & Guerri, M. (2017). Global thermal models of the lithosphere. *Geophysical Journal International*, *210*(1), 56–72.

Cho, H.-M., Kim, H.-J., Jou, H.-T., Hong, J.-K., & Baag, C.-E. (2004). Transition from rifted continental to oceanic crust at the southeastern korean margin in the east sea (japan sea). *Geophysical Research Letters*, *31*(7).

Christensen, N. I., & Mooney, W. D. (1995). Seismic velocity structure and composition of the continental crust: A global view. *Journal of Geophysical Research: Solid Earth*, *100*(B6), 9761–9788.

Connolly, J. A. D. (2005). Computation of phase equilibria by linear programming: A tool for geodynamic modeling and its application to subduction zone decarbonation. *Earth and Planetary Science Letters*, *236*(1), 524-541. doi: 10.1016/j.epsl.2005.04.033

Ducea, M. N. (2011). Fingerprinting orogenic delamination. *Geology*, *39*(2), 191–192.

Fountain, D. M., Furlong, K. P., & Salisbury, M. H. (1987). A heat production model

of a shield area and its implications for the heat flow-heat production relationship. *Geophysical Research Letters*, *14*(3), 283–286.

Gao, Y., Tilmann, F., van Herwaarden, D.-P., Thrastarson, S., Fichtner, A., Heit, B., ... Schurr, B. D. (2021). Full waveform inversion beneath the central andes: Insight into the dehydration of the nazca slab and delamination of the back-arc lithosphere. *Earth and Space Science Open Archive ESSOAr*.

Gaschnig, R. M., Rudnick, R. L., McDonough, W. F., Kaufman, A. J., Valley, J. W., Hu, Z., ... Beck, M. L. (2016). Compositional evolution of the upper continental crust through time, as constrained by ancient glacial diamictites. *Geochimica et Cosmochimica Acta*, *186*, 316–343.

Gohl, K. (2008). Antarctica's continent-ocean transitions: consequences for tectonic reconstructions. In *Antarctica: A keystone in a changing world: Proceedings of the 10th international symposium on antarctic earth sciences/alan k. cooper, peter barrett, howard stagg, bryan storey, edmund stump, woody wise, and the 10th isaes editorial team, polar resear* (pp. 29–38).

Gruber, B., Chacko, T., Pearson, D. G., Currie, C., & Menzies, A. (2021). Heat production and m oho temperatures in cratonic crust: evidence from lower crustal xenoliths from the slave craton. *Lithos*, *380*, 105889.

Hacker, B. R., & Abers, G. A. (2004). Subduction Factory 3: An Excel worksheet and macro for calculating the densities, seismic wave speeds, and H2O contents of minerals and rocks at pressure and temperature. *Geochemistry, Geophysics, Geosystems*, *5*(1). doi: 10.1029/2003GC000614

Hacker, B. R., Kelemen, P. B., & Behn, M. D. (2015). Continental lower crust. *Annual*

Review of Earth and Planetary Sciences, *43*, 167–205.

Hartmann, J., Dürr, H. H., Moosdorf, N., Meybeck, M., & Kempe, S. (2012). The geochemical composition of the terrestrial surface (without soils) and comparison with the upper continental crust. *International Journal of Earth Sciences*, *101*(1), 365–376.

Hirata, N., Karp, B. Y., Yamaguchi, T., Kanazawa, T., Suyehiro, K., Kasahara, J., ... Kinoshita, H. (1992). Oceanic crust in the japan basin of the japan sea by the 1990 japan-ussr expedition. *Geophysical Research Letters*, *19*(20), 2027–2030.

Holland, T. J. B., & Powell, R. (2004). An internally consistent thermodynamic data set for phases of petrological interest: An Internally Consistent Thermodynamic Dataset. *Journal of Metamorphic Geology*, *16*(3), 309-343. doi: 10.1111/j.1525-1314 .1998.00140.x

Huang, Y., Chubakov, V., Mantovani, F., Rudnick, R. L., & McDonough, W. F. (2013). A reference Earth model for the heat-producing elements and associated geoneutrino flux. *Geochemistry, Geophysics, Geosystems*, *14*(6), 2003-2029. doi: 10.1002/ggge .20129

Jagoutz, O., Müntener, O., Schmidt, M. W., & Burg, J.-P. (2011). The roles of flux-and decompression melting and their respective fractionation lines for continental crust formation: Evidence from the kohistan arc. *Earth and Planetary Science Letters*, *303*(1-2), 25–36.

Jagoutz, O., & Schmidt, M. W. (2012). The formation and bulk composition of modern juvenile continental crust: The kohistan arc. *Chemical Geology*, *298*, 79–96.

Jaupart, C., Mareschal, J., & Watts, A. (2007). Heat flow and thermal structure of the

lithosphere. *Treatise on geophysics*, *6*, 217–252.

Jaupart, C., Mareschal, J.-C., Bouquerel, H., & Phaneuf, C. (2014). The building and stabilization of an archean craton in the superior province, canada, from a heat flow perspective. *Journal of Geophysical Research: Solid Earth*, *119*(12), 9130–9155.

Jaupart, C., Mareschal, J.-C., & Iarotsky, L. (2016). Radiogenic heat production in the continental crust. *Lithos*, *262*, 398–427.

Kay, R. W., & Kay, S. M. (1993). Delamination and delamination magmatism. *Tectonophysics*, *219*(1-3), 177–189.

Kukkonen, I., Golovanova, I., Khachay, Y. V., Druzhinin, V., Kosarev, A., & Schapov, V. (1997). Low geothermal heat flow of the urals fold belt—implication of low heat production, fluid circulation or palaeoclimate? *Tectonophysics*, *276*(1-4), 63–85.

Liu, Y.-S., Gao, S., Jin, S.-Y., Hu, S.-H., Sun, M., Zhao, Z.-B., & Feng, J.-L. (2001). Geochemistry of lower crustal xenoliths from neogene hannuoba basalt, north china craton: Implications for petrogenesis and lower crustal composition. *Geochimica et Cosmochimica Acta*, *65*(15), 2589–2604.

Lucazeau, F. (2019). Analysis and mapping of an updated terrestrial heat flow data set. *Geochemistry, Geophysics, Geosystems*, *20*(8), 4001–4024.

Mareschal, J.-C., & Jaupart, C. (2013). Radiogenic heat production, thermal regime and evolution of continental crust. *Tectonophysics*, *609*, 524–534.

McCarthy, A., Falloon, T., Sauermilch, I., Whittaker, J., Niida, K., & Green, D. (2020). Revisiting the australian-antarctic ocean-continent transition zone using petrological and geophysical characterization of exhumed subcontinental mantle. *Geochemistry, Geophysics, Geosystems*, *21*(7), e2020GC009040.

Miao, S. Q., Li, H. P., & Chen, G. (2014). Temperature dependence of thermal diffusivity, specific heat capacity, and thermal conductivity for several types of rocks. *Journal of Thermal Analysis and Calorimetry*, *115*(2), 1057–1063.

Mooney, W. (2015). *Global crustal structure* (G. Schubert, Ed.). Elsevier.

Mooney, W. D., Laske, G., & Masters, T. G. (1998). Crust 5.1: A global crustal model at 5× 5. *Journal of Geophysical Research: Solid Earth*, *103*(B1), 727–747.

Nelson, K. D., Zhao, W., Brown, L., Kuo, J., Che, J., Liu, X., ... others (1996). Partially molten middle crust beneath southern tibet: synthesis of project indepth results. *Science*, *274*(5293), 1684–1688.

Nyblade, A. A., & Pollack, H. N. (1993). A global analysis of heat flow from precambrian terrains: implications for the thermal structure of archean and proterozoic lithosphere. *Journal of Geophysical Research: Solid Earth*, *98*(B7), 12207–12218.

Pasyanos, M. E., Masters, T. G., Laske, G., & Ma, Z. (2014). LITHO1.0: An updated crust and lithospheric model of the Earth. *Journal of Geophysical Research: Solid Earth*, *119*(3), 2153-2173. doi: 10.1002/2013JB010626

Phaneuf, C., & Mareschal, J.-C. (2014). Estimating concentrations of heat producing elements in the crust near the sudbury neutrino observatory, ontario, canada. *Tectonophysics*, *622*, 135–144.

Pinet, C., & Jaupart, C. (1987). The vertical distribution of radiogenic heat production in the precambrian crust of norway and sweden: geothermal implications. *Geophysical Research Letters*, *14*(3), 260–263.

Regis, D., Warren, C., Mottram, C. M., & Roberts, N. M. (2016). Using monazite and zircon petrochronology to constrain the P–T–t evolution of the middle crust in the

bhutan himalaya. *Journal of Metamorphic Geology*, *34*(6), 617–639.

Ries, J., Bettadpur, S., Eanes, R., Kang, Z., Ko, U.-d., McCullough, C., ... others (2016). *The development and evaluation of the global gravity model ggm05* (Tech. Rep.). Center for Space Research, Report number: CSR-16-02 NASA.

Rudnick, R. L., & Gao, S. (2014). Composition of the Continental Crust. In *Treatise on Geochemistry* (p. 1-51). Elsevier. doi: 10.1016/B978-0-08-095975-7.00301-6

Rudnick, R. L., & Nyblade, A. A. (1999). The thickness and heat production of archean lithosphere: constraints from xenolith thermobarometry and surface heat flow. *Mantle petrology: field observations and high pressure experimentation: a tribute to Francis R.(Joe) Boyd*, *6*, 3–12.

Sammon, L. G., Gao, C., & McDonough, W. F. (2020). Lower crustal composition in the southwestern united states. *Journal of Geophysical Research: Solid Earth*, *125*(3), e2019JB019011.

Sammon, L. G., & McDonough, W. F. (2021). A geochemical review of amphibolite, granulite, and eclogite facies lithologies: Perspectives on the deep continental crust.

Schilling, F., & Partzsch, G. (2001). Quantifying partial melt fraction in the crust beneath the central andes and the tibetan plateau. *Physics and Chemistry of the Earth, Part A: Solid Earth and Geodesy*, *26*(4-5), 239–246.

Schmitz, M., Heinsohn, W.-D., & Schilling, F. (1997). Seismic, gravity and petrological evidence for partial melt beneath the thickened central andean crust (21–23 s). *Tectonophysics*, *270*(3-4), 313–326.

Searle, M., Cottle, J., Streule, M., & Waters, D. (2009). Crustal melt granites and migmatites along the himalaya: melt source, segregation, transport and granite em-

placement mechanisms. *Earth and Environmental Science Transactions of the Royal Society of Edinburgh*, *100*(1-2), 219–233.

Semprich, J., & Simon, N. S. C. (2014). Inhibited eclogitization and consequences for geophysical rock properties and delamination models: Constraints from cratonic lower crustal xenoliths. *Gondwana Research*, *25*(2), 668-684. doi: 10.1016/j.gr.2012.08.018

Shen, W., Wiens, D. A., Lloyd, A. J., & Nyblade, A. A. (2020). A geothermal heat flux map of antarctica empirically constrained by seismic structure. *Geophysical Research Letters*, *47*(14), e2020GL086955.

Stixrude, L., & Lithgow-Bertelloni, C. (2011). Thermodynamics of mantle minerals-ii. phase equilibria. *Geophysical Journal International*, *184*(3), 1180–1213.

Szwillus, W., Afonso, J. C., Ebbing, J., & Mooney, W. D. (2019). Global crustal thickness and velocity structure from geostatistical analysis of seismic data. *Journal of Geophysical Research: Solid Earth*, *124*(2), 1626-1652.

Wilkinson, B. H., McElroy, B. J., Kesler, S. E., Peters, S. E., & Rothman, E. D. (2009). Global geologic maps are tectonic speedometers—rates of rock cycling from area-age frequencies. *Geological Society of America Bulletin*, *121*(5-6), 760–779.

Wipperfurth, S. A., Guo, M., Šrámek, O., & McDonough, W. F. (2018). Earth's chondritic Th/U: Negligible fractionation during accretion, core formation, and crust–mantle differentiation. *Earth and Planetary Science Letters*, *498*, 196-202. doi: 10.1016/j.epsl.2018.06.029

Wipperfurth, S. A., Šrámek, O., & McDonough, W. F. (2020). Reference models for lithospheric geoneutrino signal. *Journal of Geophysical Research: Solid Earth*, *125*(2),

e2019JB018433.

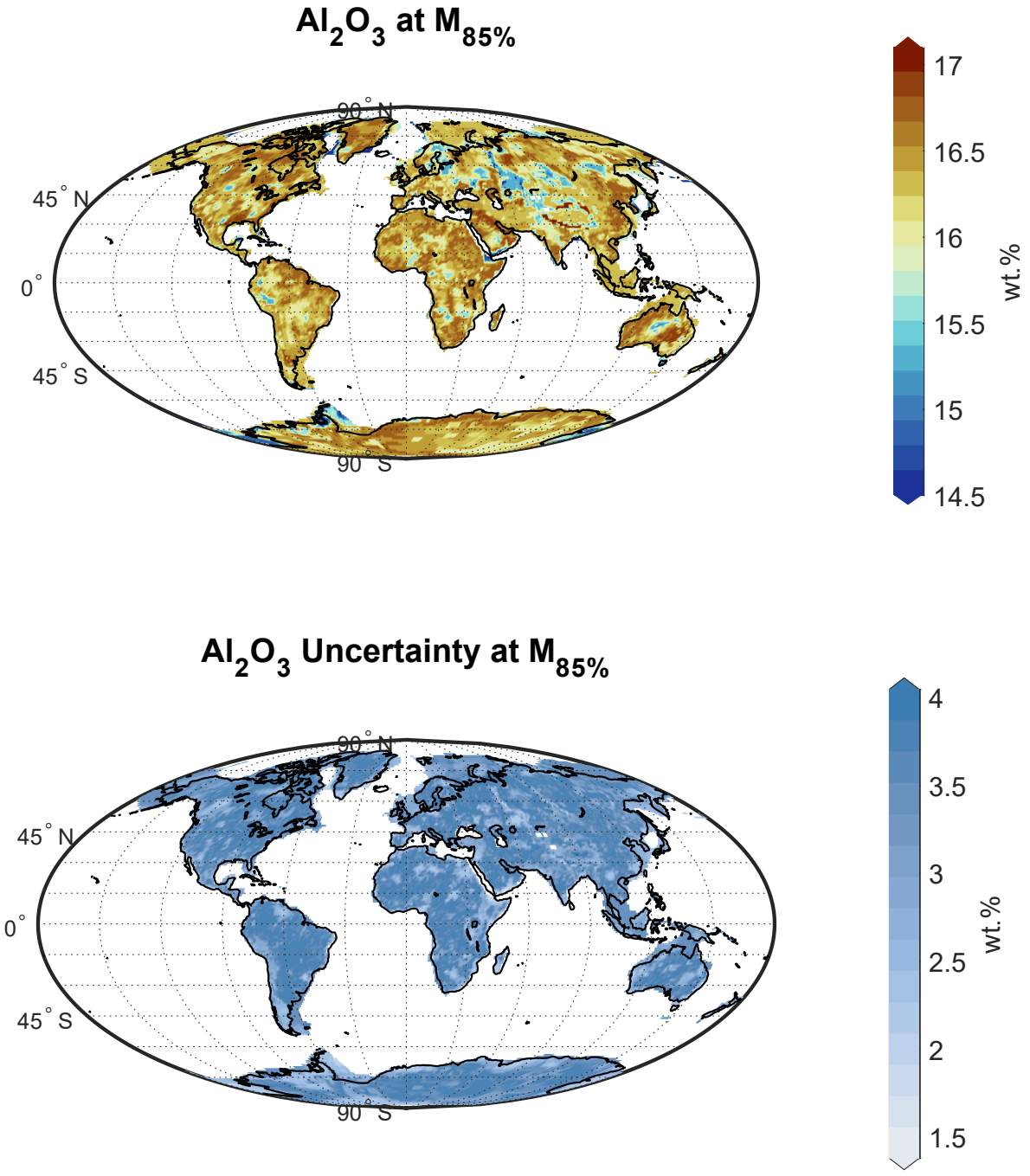
Al2O3 at M85%
90° N
45° N
0°
45° S
90° S
17
16.5
16
15.5
15
14.5
wt.%
Al2O3 Uncertainty at M85%
90° N
45° N
0°
45° S
90° S
4
3.5
3
2.5
2
1.5
wt.%

Figure S1.

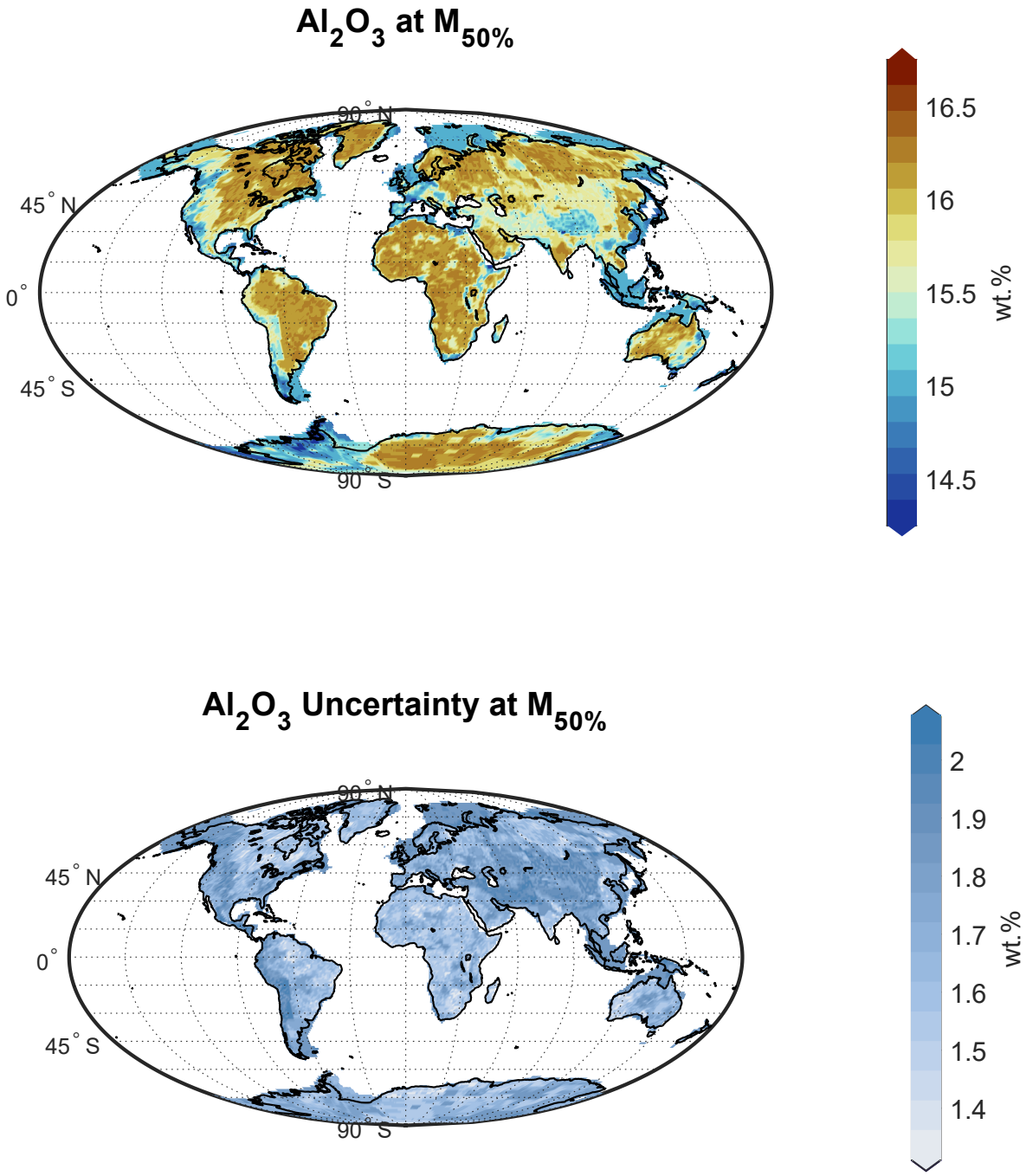
Al2O3 at M50%
90° N
45° N
0°
45° S
90° S
16.5
16
15.5
15
14.5
wt.%
Al2O3 Uncertainty at M50%
90° N
45° N
0°
45° S
90° S
2
1.9
1.8
1.7
1.6
1.5
1.4
wt.%

Figure S2.

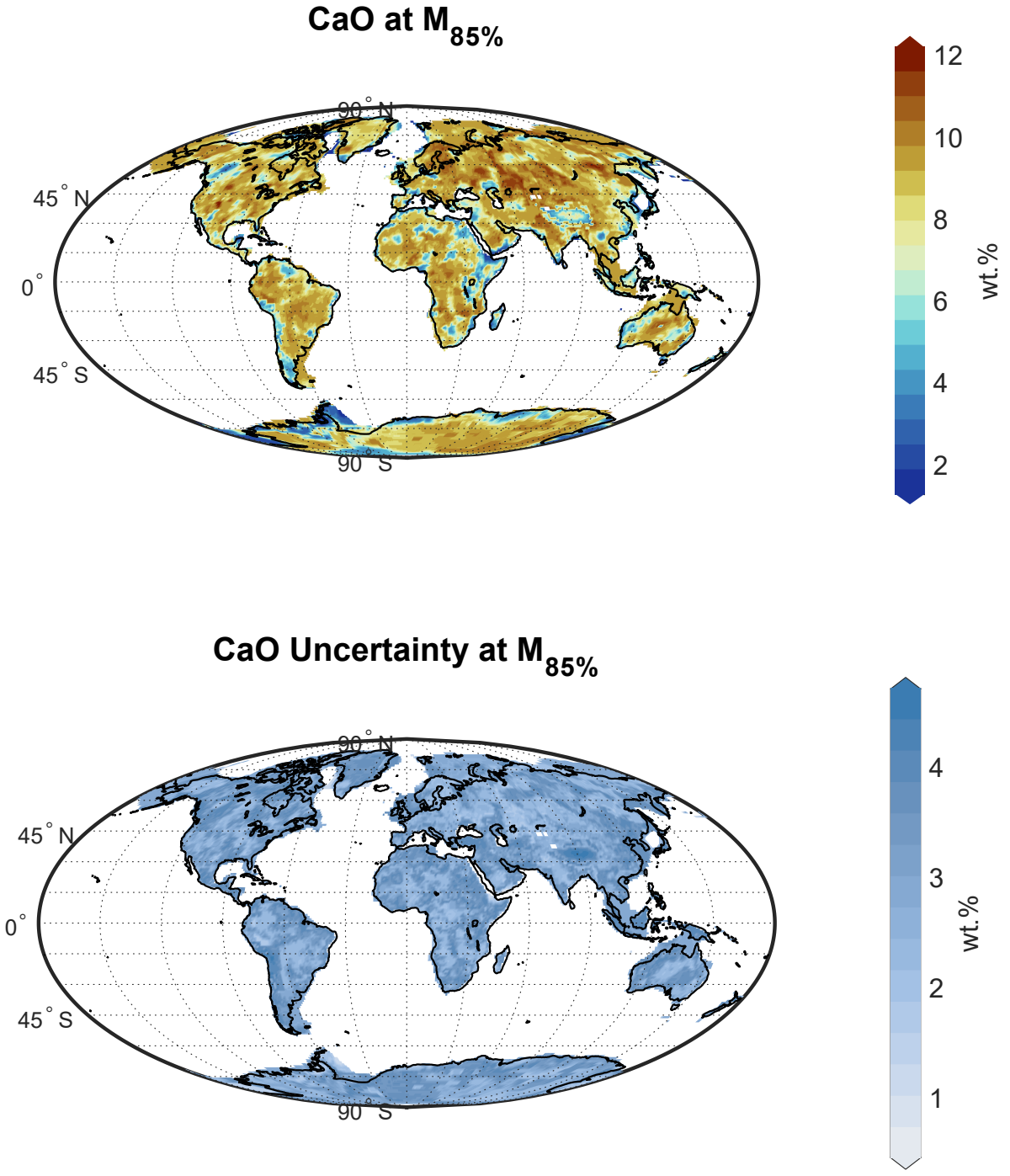
CaO at M85%
90° N
45° N
0°
45° S
90° S
12
10
8
6
4
2
wt.%
CaO Uncertainty at M85%
90° N
45° N
0°
45° S
90° S
4
3
2
1
wt.%

Figure S3.

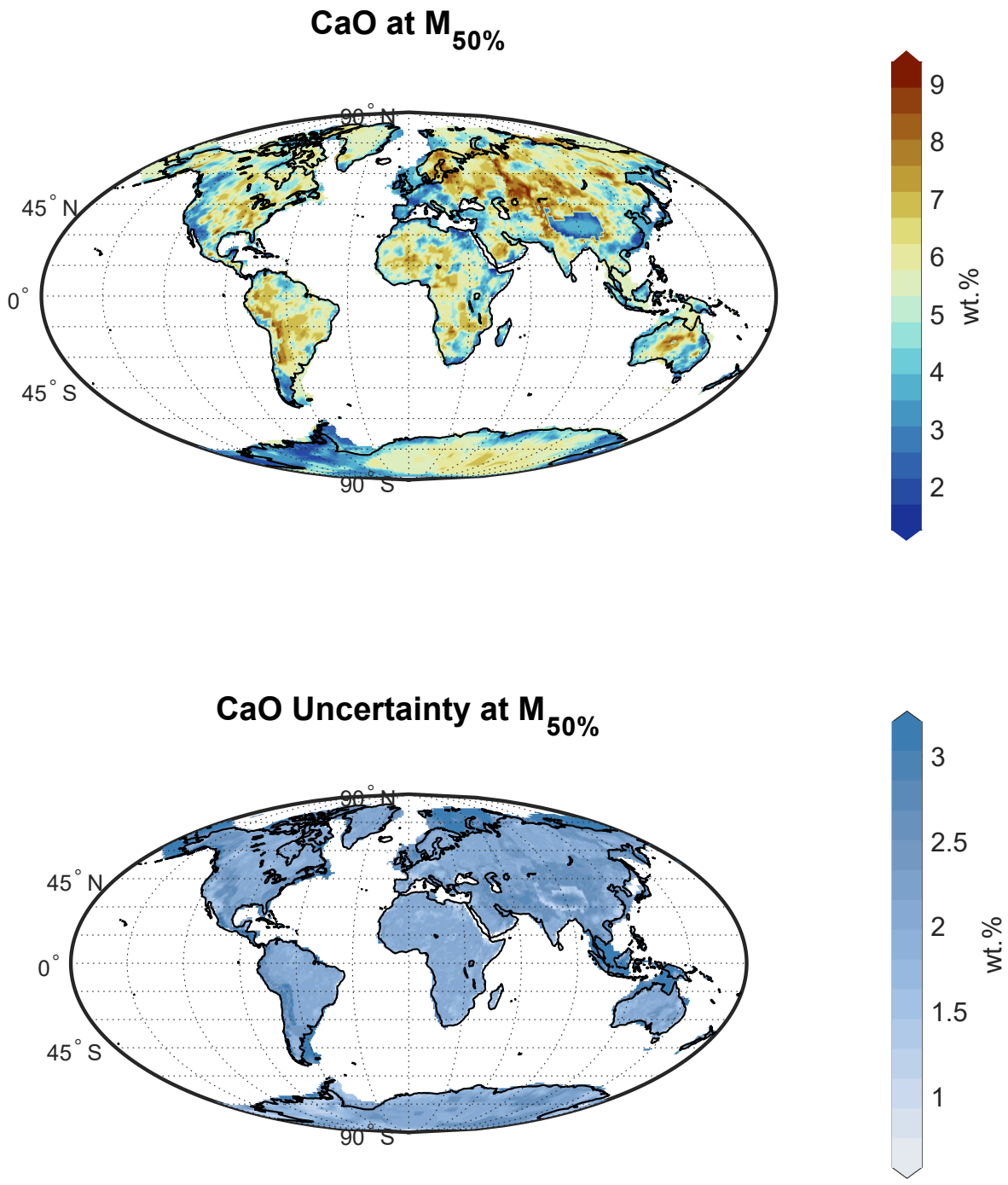
CaO at M50%
90° N
45° N
0°
45° S
90° S
9
8
7
6
5
4
3
2
wt.%
CaO Uncertainty at M50%
90° N
45° N
0°
45° S
90° S
3
2.5
2
1.5
1
wt.%

Figure S4.

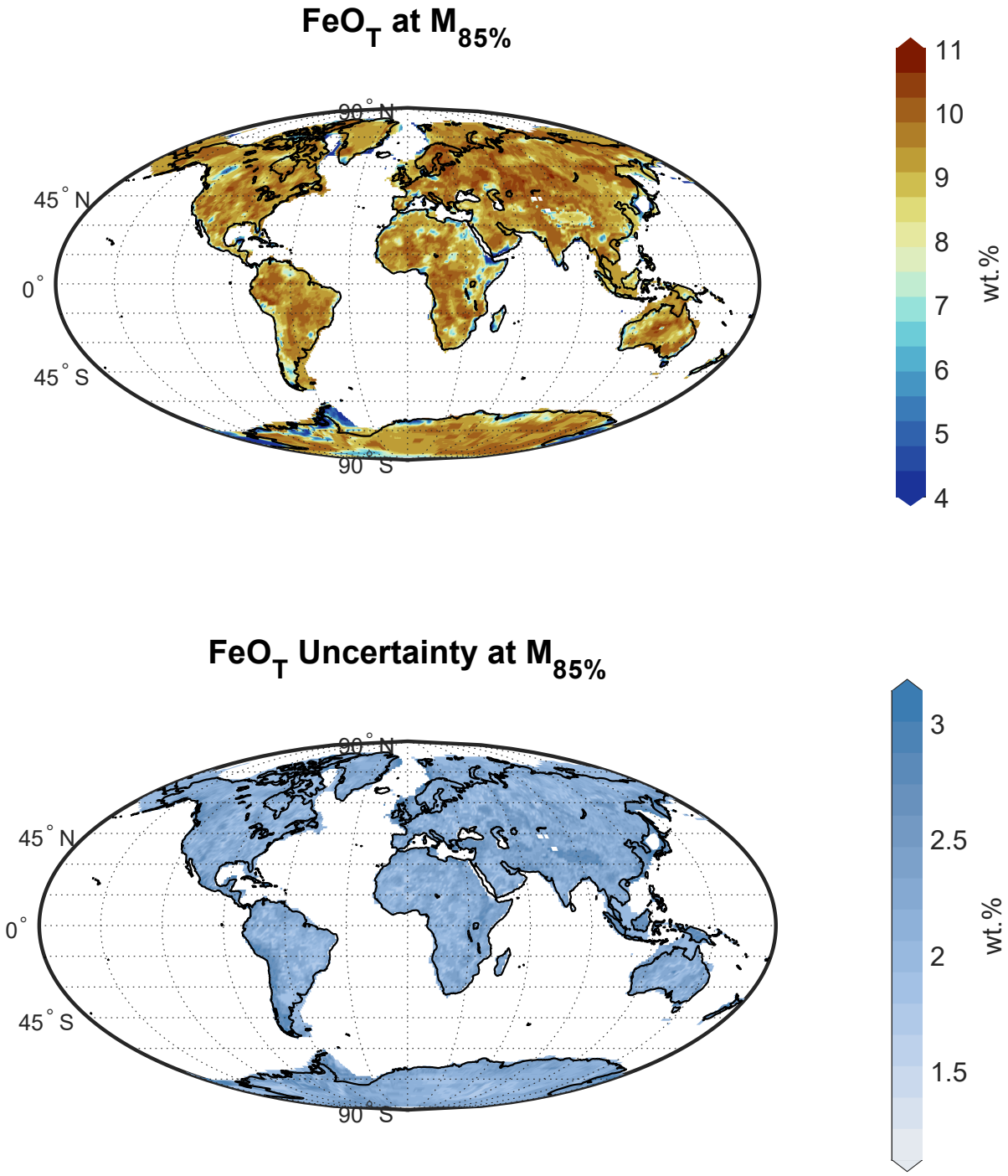
FeO$_T$ at M$_{85\%}$
90° N
45° N
0°
45° S
90° S
11
10
9
8
7
6
5
4
wt.%
FeO$_T$ Uncertainty at M$_{85\%}$
90° N
45° N
0°
45° S
90° S
3
2.5
2
1.5
wt.%

Figure S5.

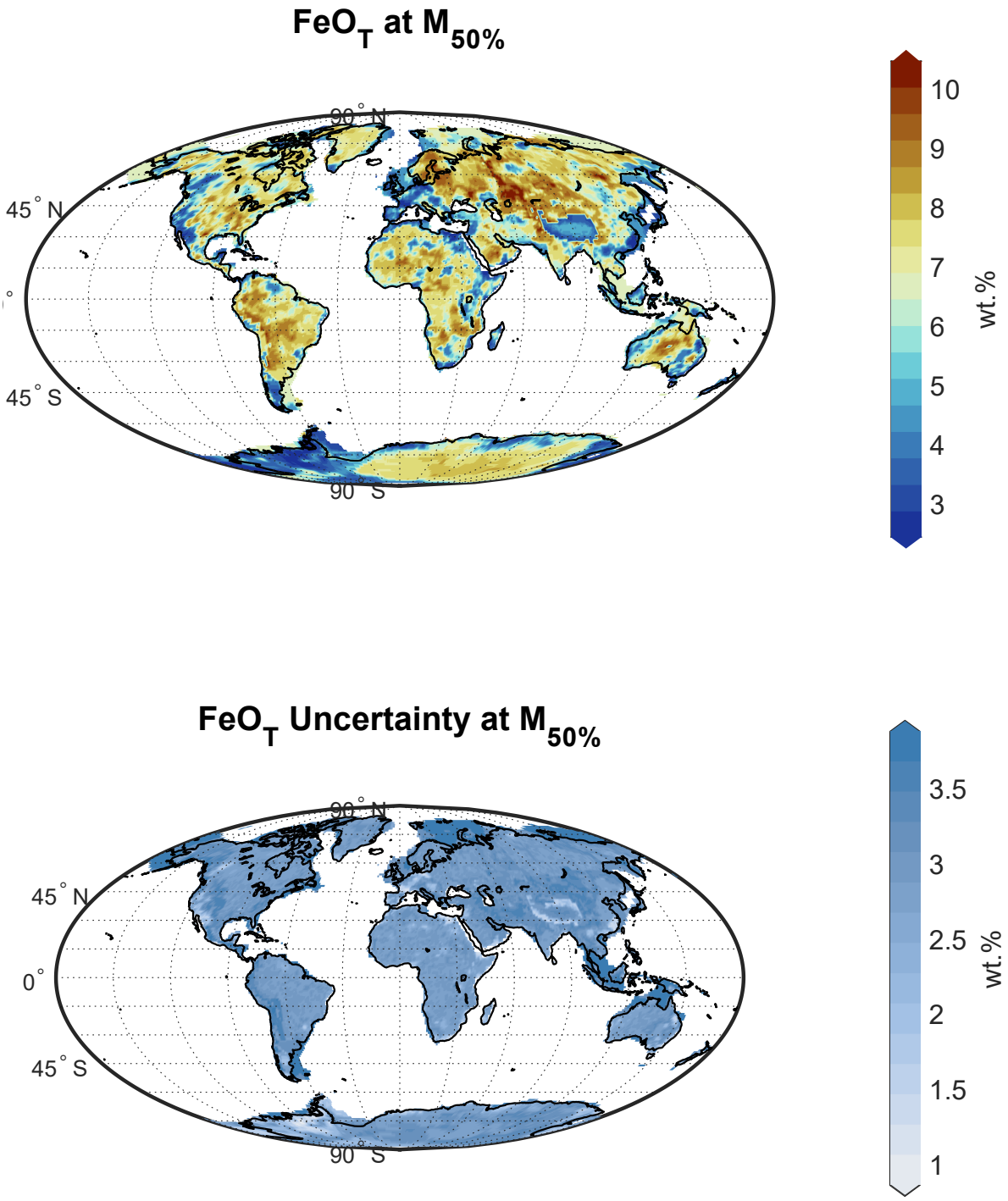
FeO$_T$ at M$_{50\%}$
90° N
45° N
0°
45° S
90° S
10
9
8
7
6
5
4
3
wt.%
FeO$_T$ Uncertainty at M$_{50\%}$
90° N
45° N
0°
45° S
90° S
3.5
3
2.5
2
1.5
1
wt.%

Figure S6.

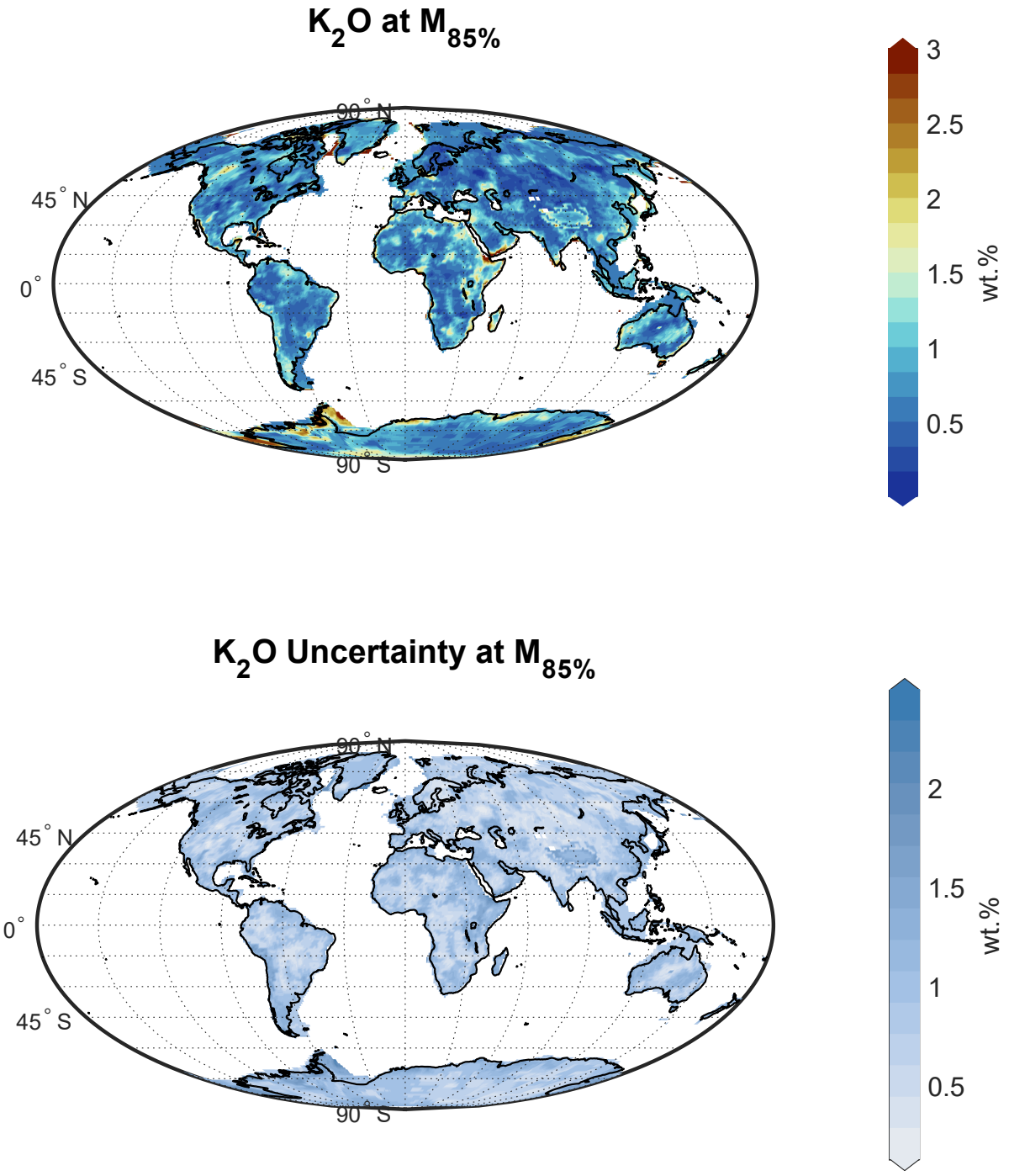
K2O at M85%
90° N
45° N
0°
45° S
90° S
3
2.5
2
1.5
1
0.5
wt.%
K2O Uncertainty at M85%
90° N
45° N
0°
45° S
90° S
2
1.5
1
0.5
wt.%

Figure S7.

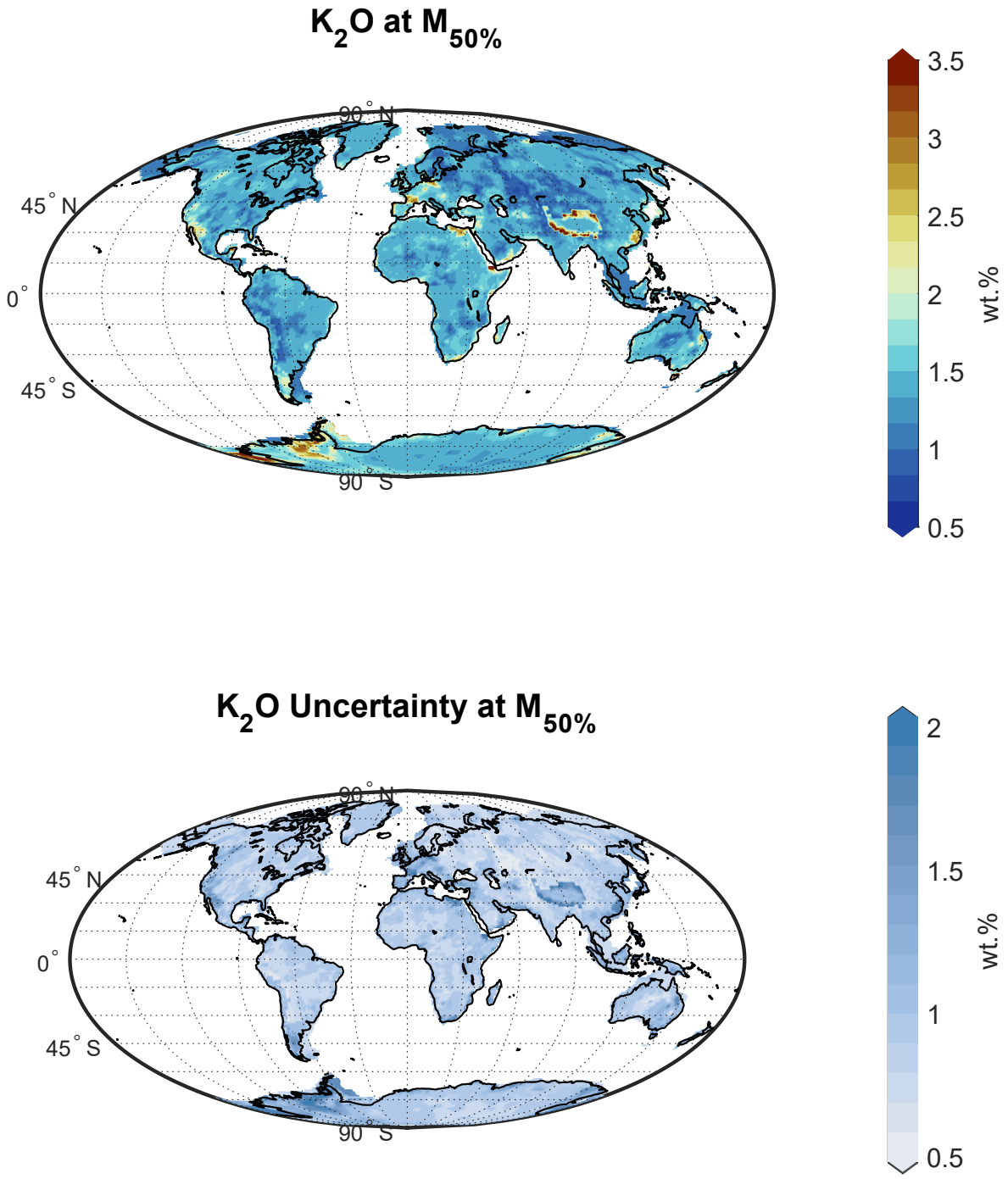
K2O at M50%
90° N
45° N
0°
45° S
90° S
3.5
3
2.5
2
1.5
1
0.5
wt.%
K2O Uncertainty at M50%
90° N
45° N
0°
45° S
90° S
2
1.5
1
0.5
wt.%

Figure S8.

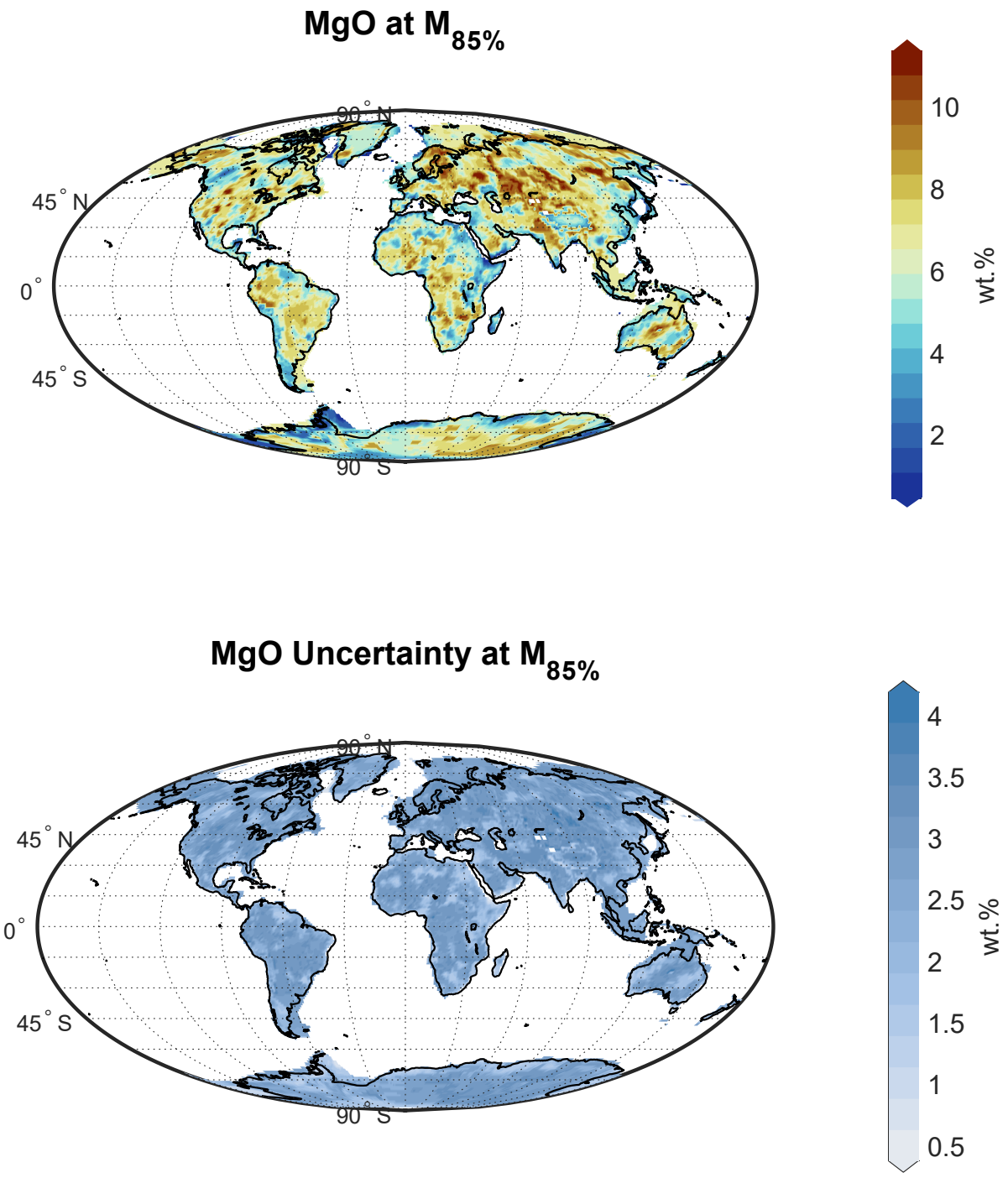
MgO at M85%
90° N
45° N
0°
45° S
90° S
10
8
6
4
2
wt.%
MgO Uncertainty at M85%
90° N
45° N
0°
45° S
90° S
4
3.5
3
2.5
2
1.5
1
0.5
wt.%

Figure S9.

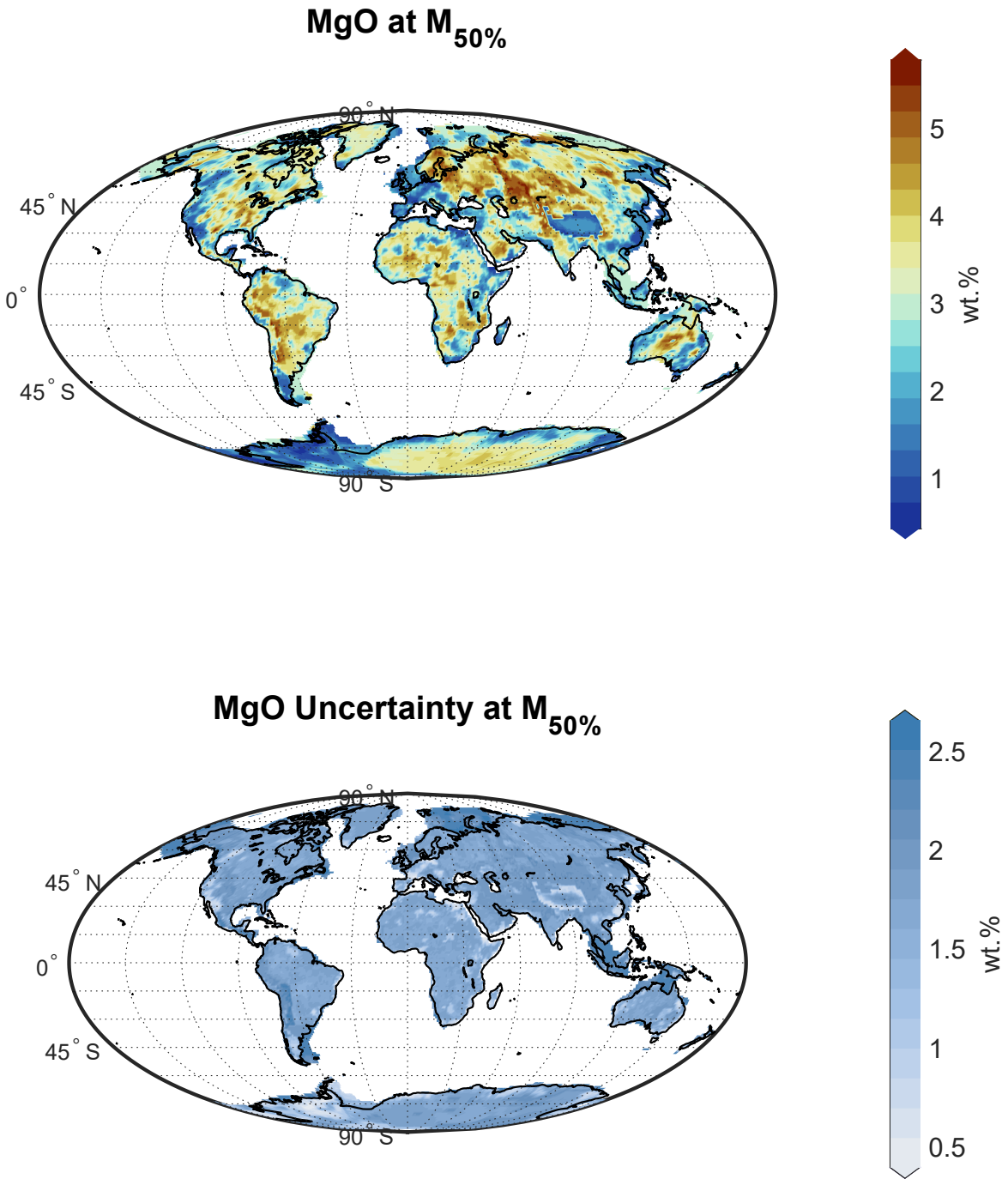
MgO at M50%
90° N
45° N
0°
45° S
90° S
5
4
3
2
1
wt.%
MgO Uncertainty at M50%
90° N
45° N
0°
45° S
90° S
2.5
2
1.5
1
0.5
wt.%

Figure S10.

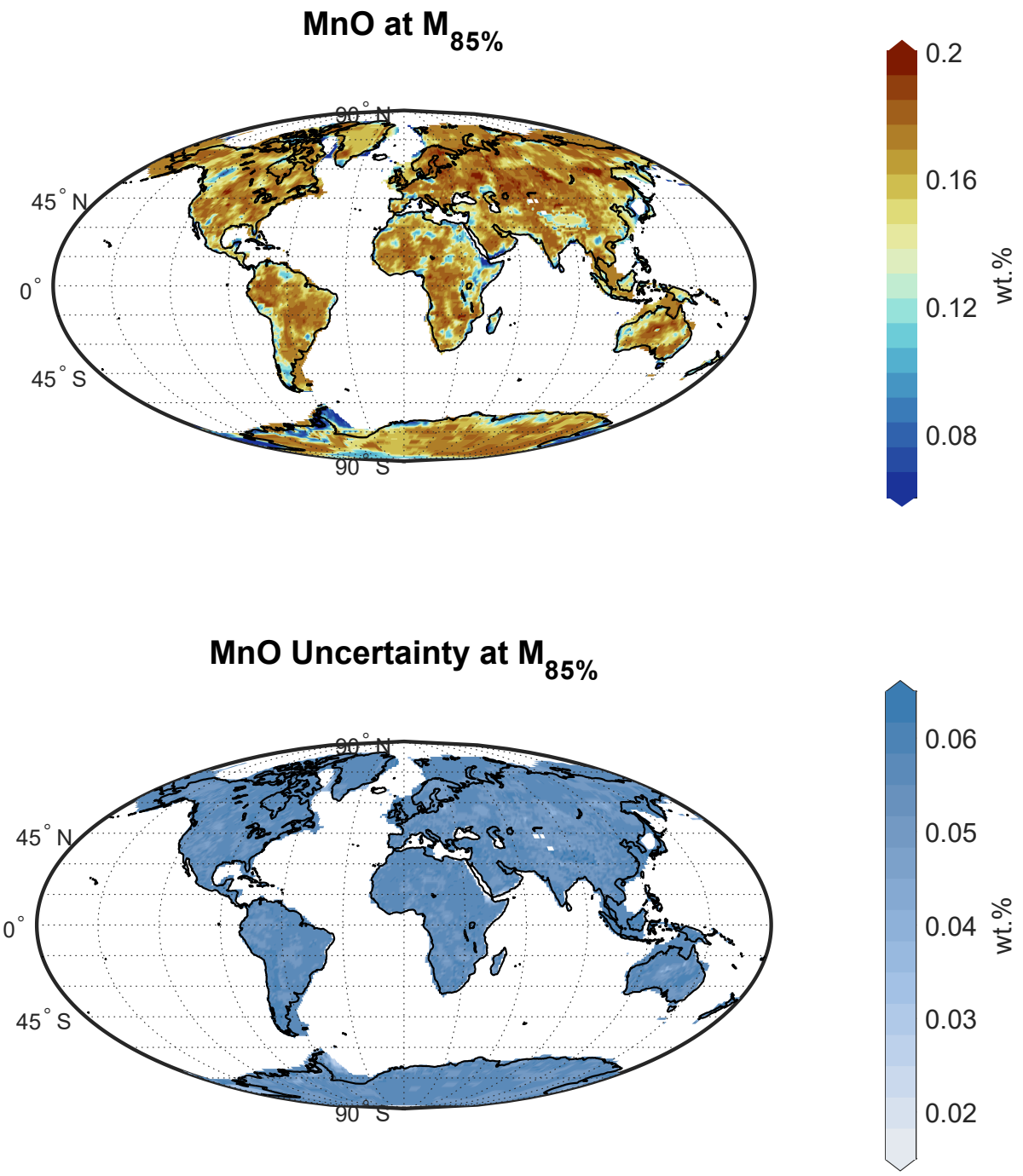
MnO at M85%
90° N
45° N
0°
45° S
90° S
0.2
0.16
0.12
0.08
wt.%
MnO Uncertainty at M85%
90° N
45° N
0°
45° S
90° S
0.06
0.05
0.04
0.03
0.02
wt.%

Figure S11.

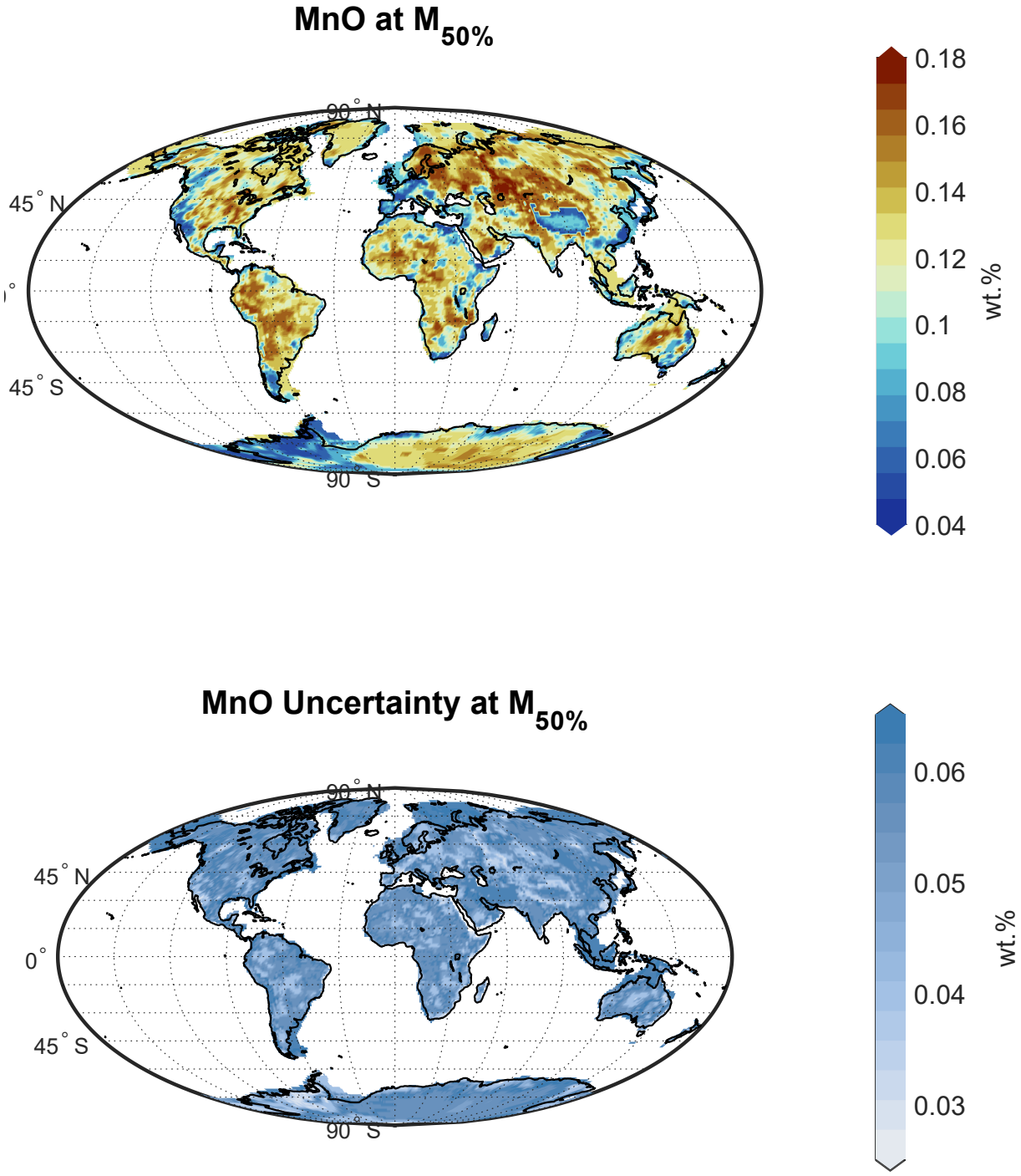
MnO at M50%
90° N
45° N
0°
45° S
90° S
0.18
0.16
0.14
0.12
0.1
0.08
0.06
0.04
wt.%
MnO Uncertainty at M50%
90° N
45° N
0°
45° S
90° S
0.06
0.05
0.04
0.03
wt.%

Figure S12.

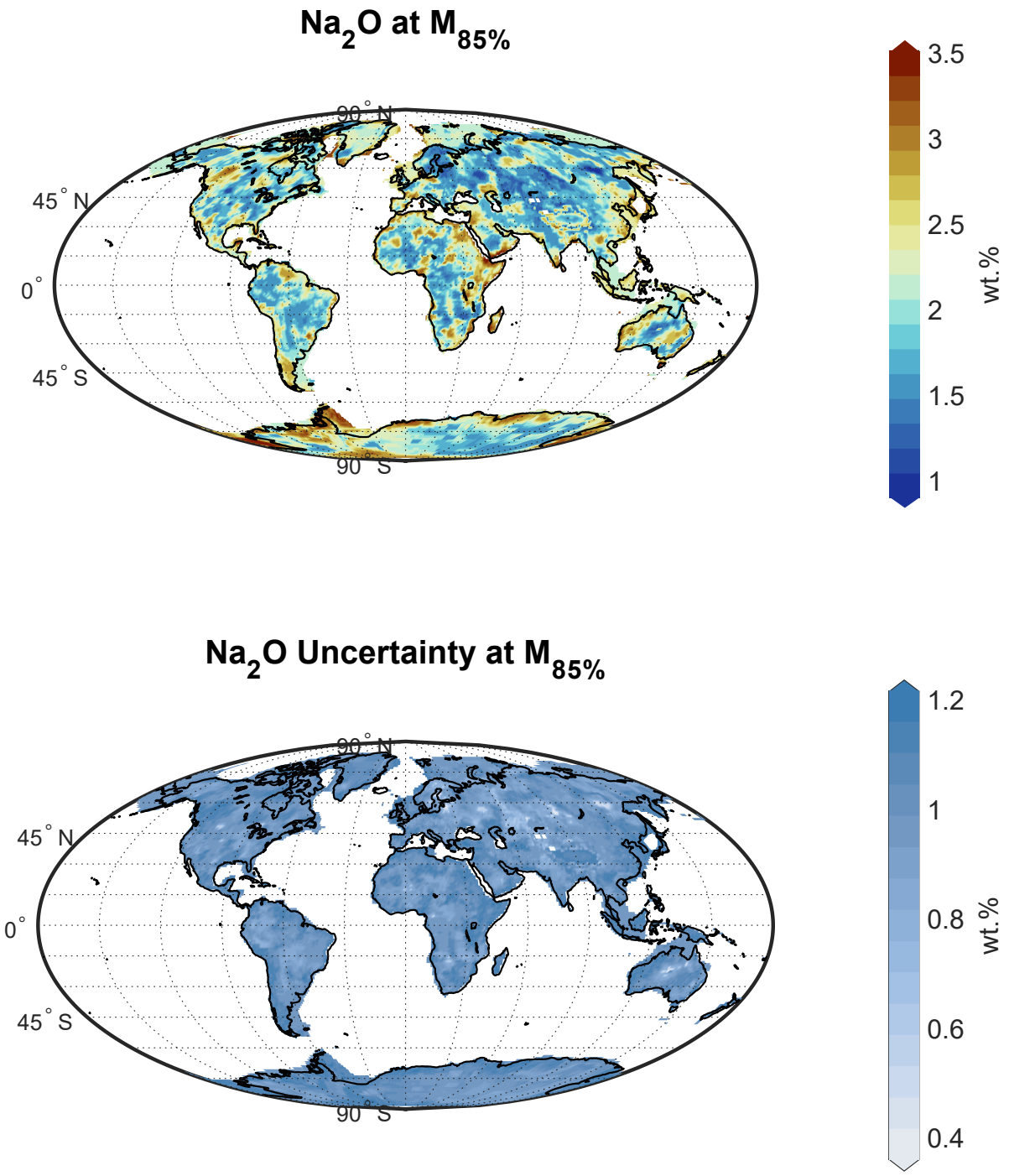
Na2O at M85%
90° N
45° N
0°
45° S
90° S
3.5
3
2.5
2
1.5
1
wt.%
Na2O Uncertainty at M85%
90° N
45° N
0°
45° S
90° S
1.2
1
0.8
0.6
0.4
wt.%

Figure S13.

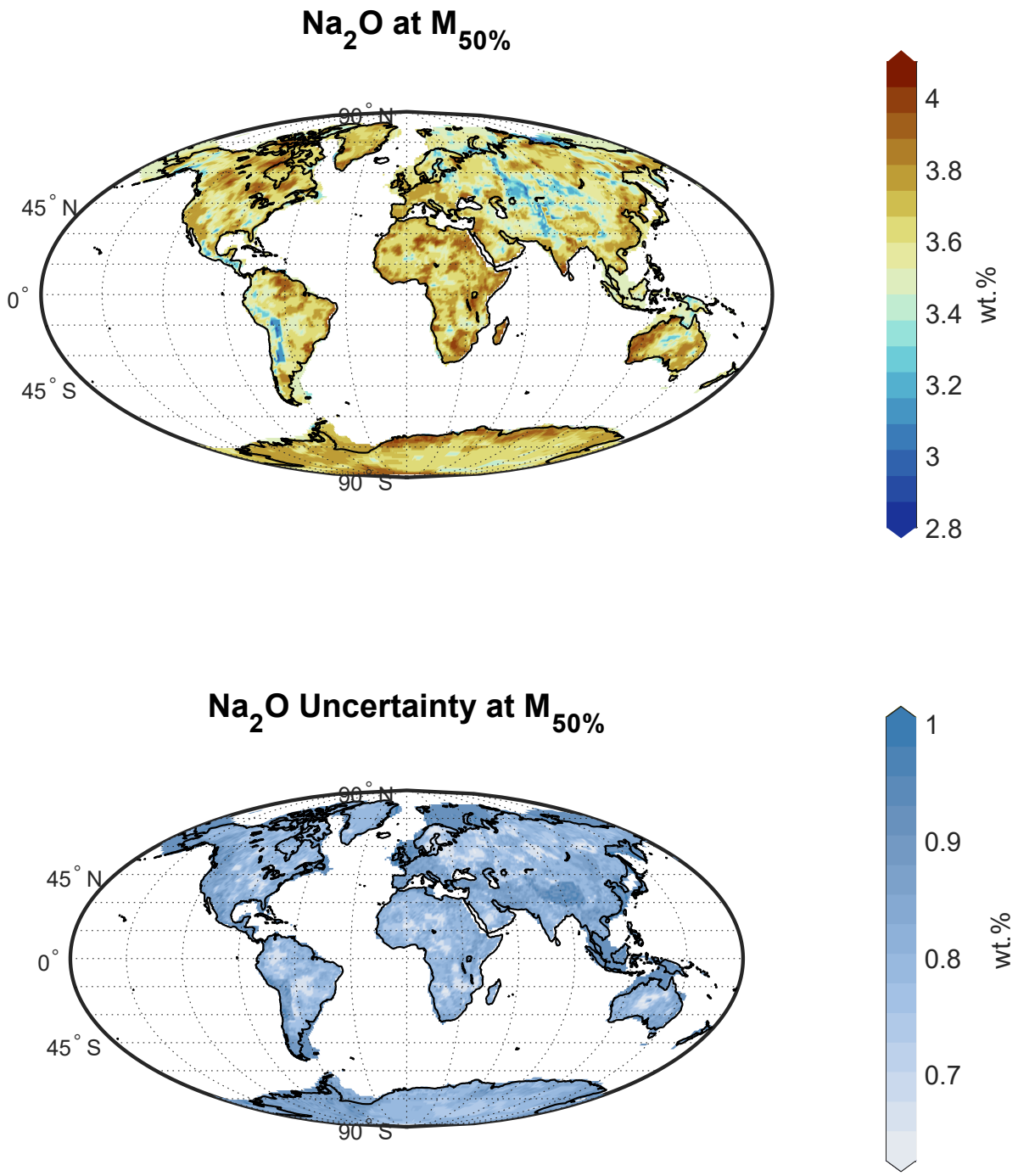
Na2O at M50%
90° N
45° N
0°
45° S
90° S
4
3.8
3.6
3.4
3.2
3
2.8
wt.%
Na2O Uncertainty at M50%
90° N
45° N
0°
45° S
90° S
1
0.9
0.8
0.7
wt.%

Figure S14.

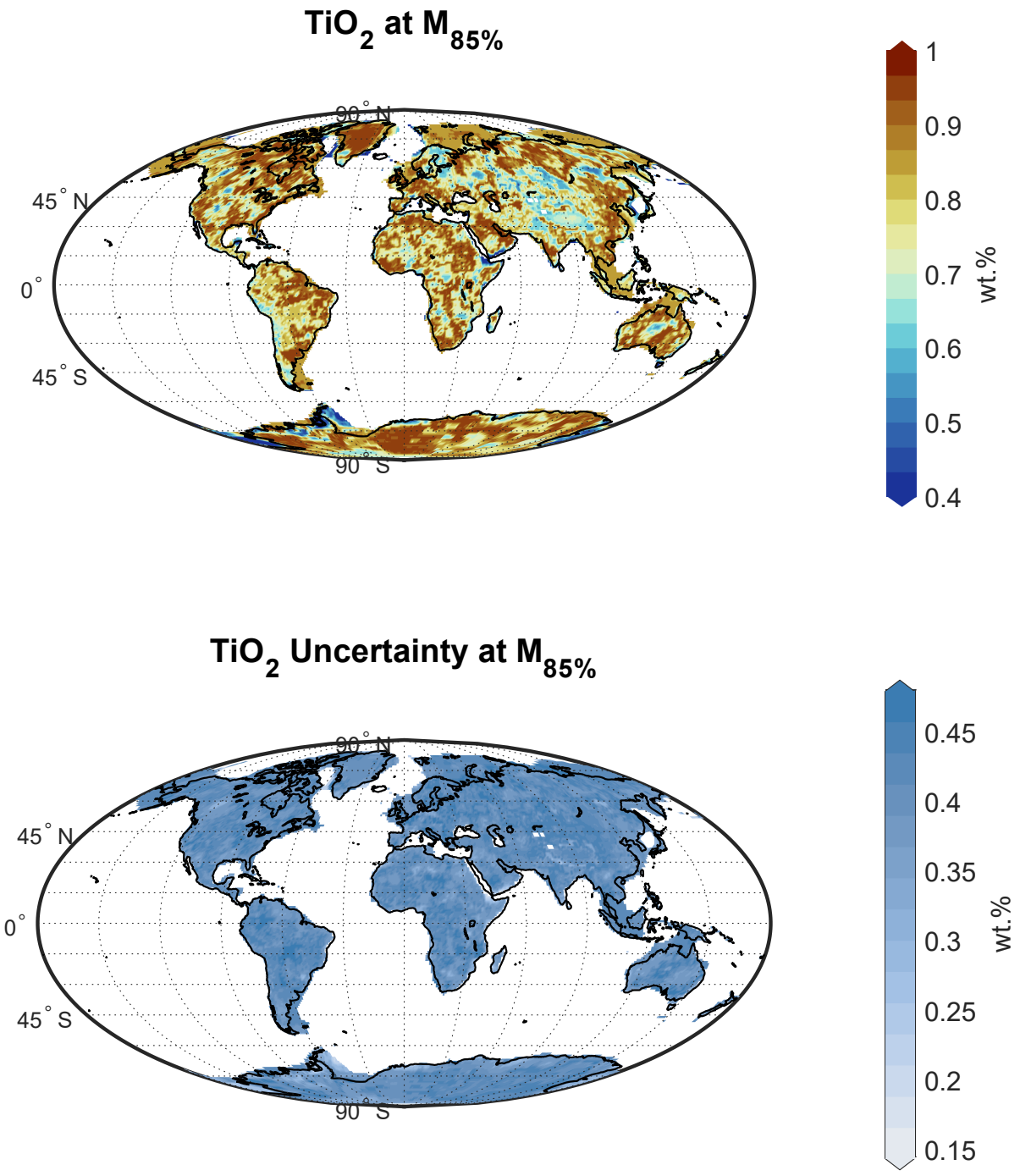
TiO2 at M85%
90° N
45° N
0°
45° S
90° S
1
0.9
0.8
0.7
0.6
0.5
0.4
wt.%
TiO2 Uncertainty at M85%
90° N
45° N
0°
45° S
90° S
0.45
0.4
0.35
0.3
0.25
0.2
0.15
wt.%

Figure S15.

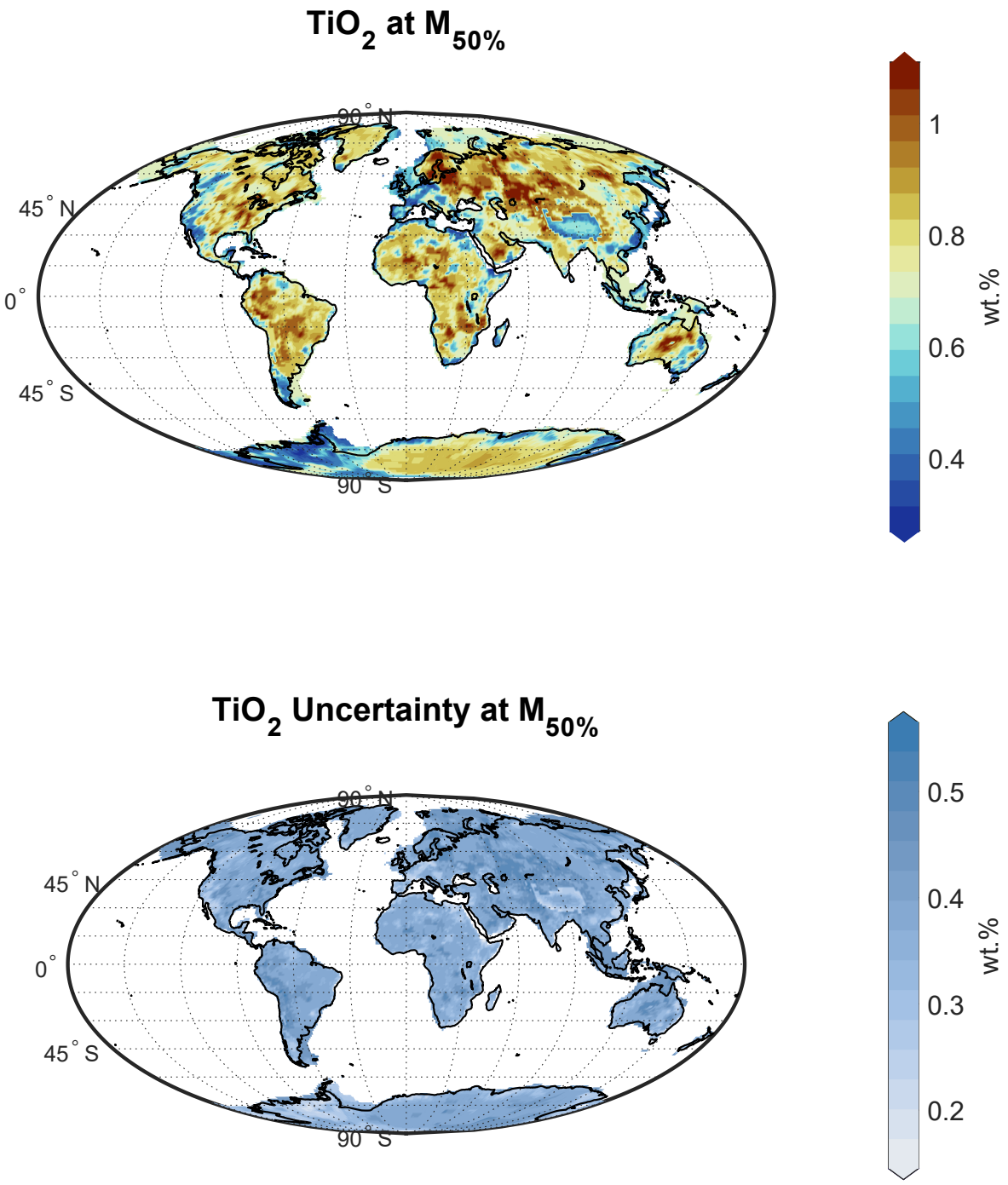
TiO2 at M50%
90° N
45° N
0°
45° S
90° S
1
0.8
0.6
0.4
wt.%
TiO2 Uncertainty at M50%
90° N
45° N
0°
45° S
90° S
0.5
0.4
0.3
0.2
wt.%

Figure S16.

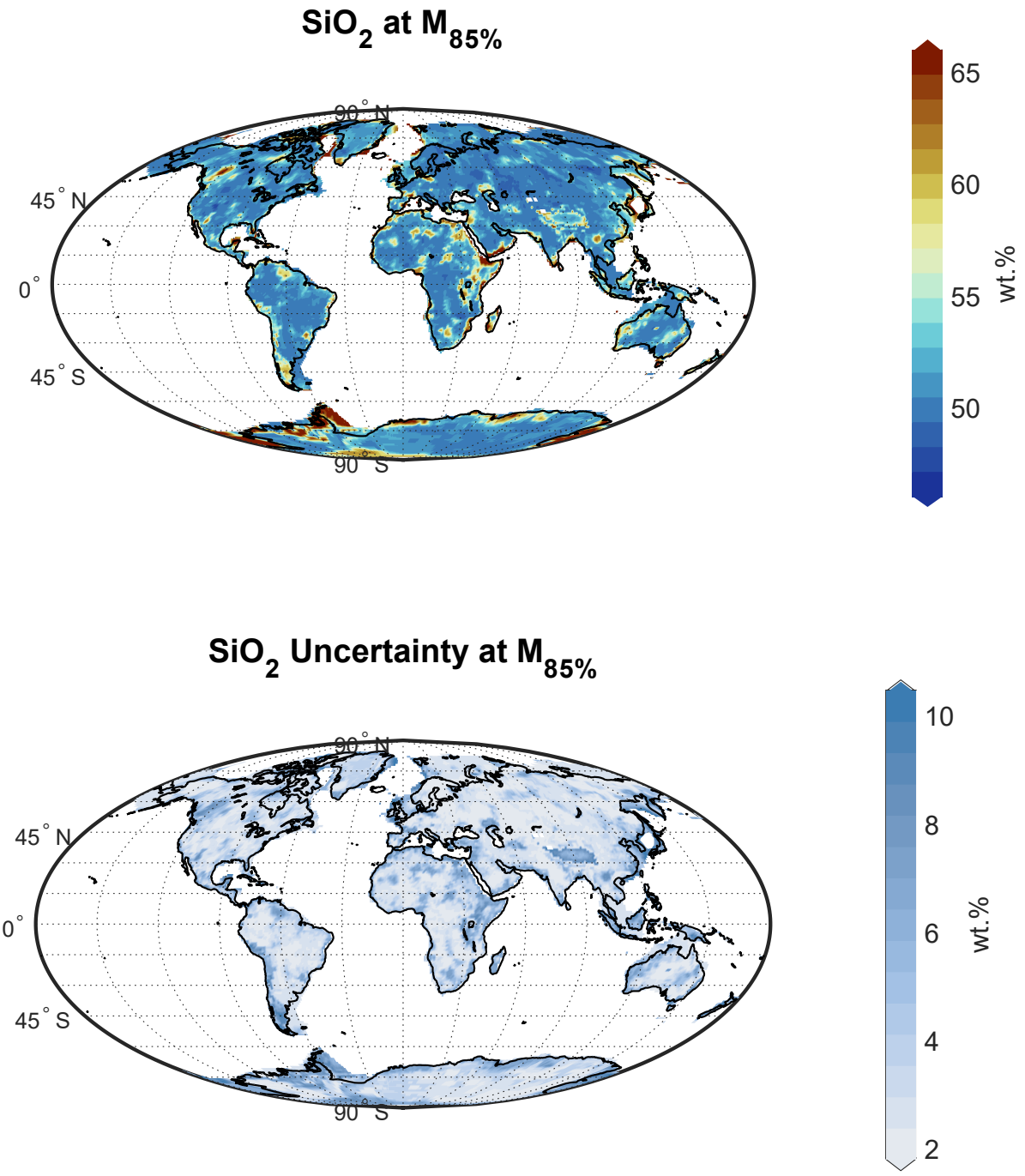
SiO2 at M85%
90° N
45° N
0°
45° S
90° S
65
60
55
50
wt.%
SiO2 Uncertainty at M85%
90° N
45° N
0°
45° S
90° S
10
8
6
4
2
wt.%

Figure S17.

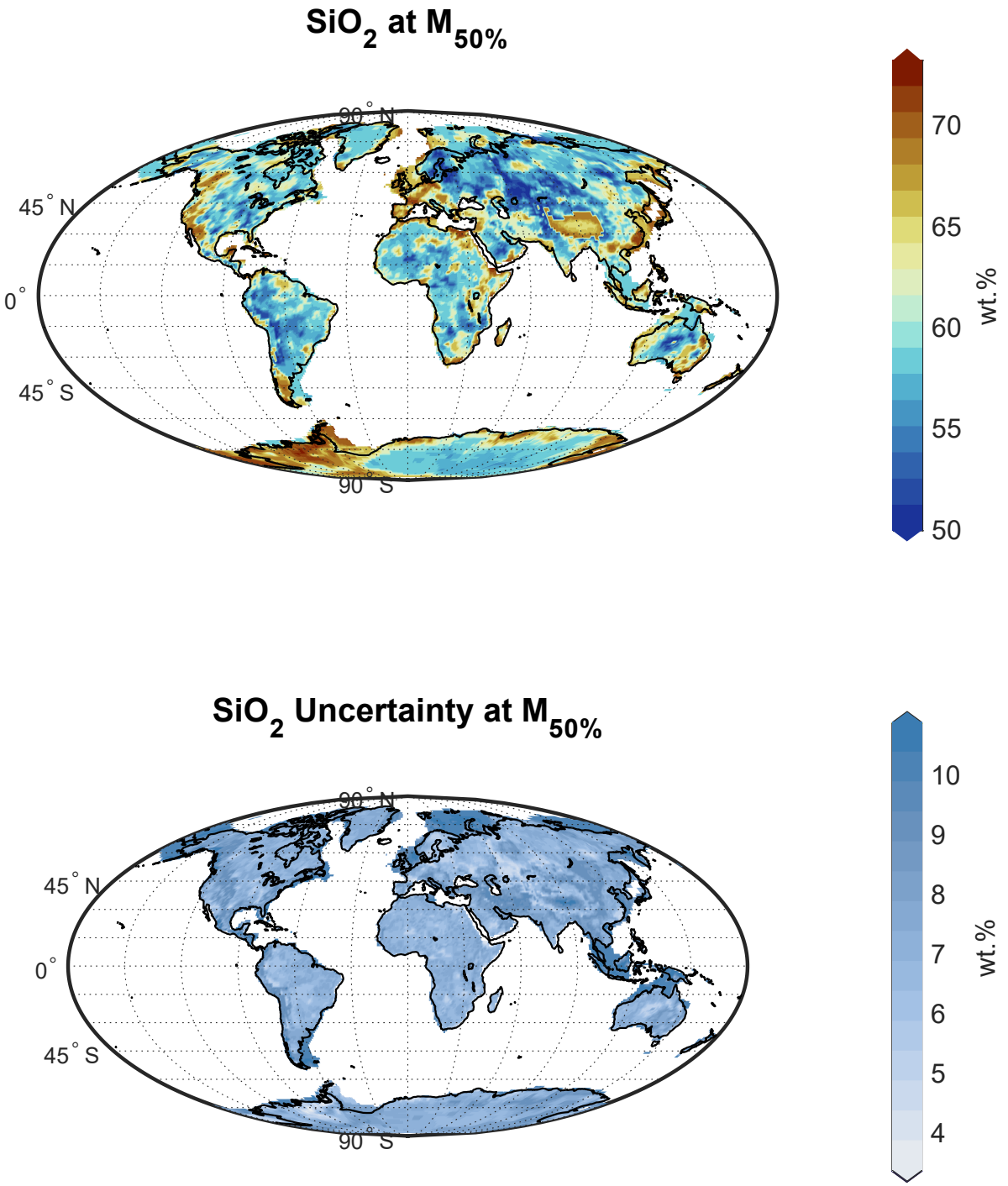
SiO2 at M50%
90° N
45° N
0°
45° S
90° S
70
65
60
55
50
wt.%
SiO2 Uncertainty at M50%
90° N
45° N
0°
45° S
90° S
10
9
8
7
6
5
4
wt.%

Figure S18.